Uncovering the hidden mechanisms of giant unilamellar vesicle formation in cDICE

Lori Van de Cauter[1,†], Yash K. Jawale[2,†], Daniel Tam[3], Lucia Baldauf[2,4], Lennard van Buren[2], Gijsje H. Koenderink[2], Marileen Dogterom[2], and Kristina A. Ganzinger[1,*]

[1]Autonomous Matter department, AMOLF, Amsterdam, The Netherlands

[2]Department of Bionanoscience, Kavli Institute of Nanoscience, Delft University of Technology, Delft, The Netherlands

[3]Laboratory for Aero and Hydrodynamics, Delft University of Technology, Delft, The Netherlands

[4]Current address: London Centre for Nanotechnology, University College London, London, United Kingdom

[†]equal contribution

[*]corresponding author: K.Ganzinger@amolf.nl

Keywords: emulsion transfer, fluid dynamics, lipid membranes, vesicles, synthetic cell

---

Graphical abstract (figure 8x4cm; text max 250 characters)

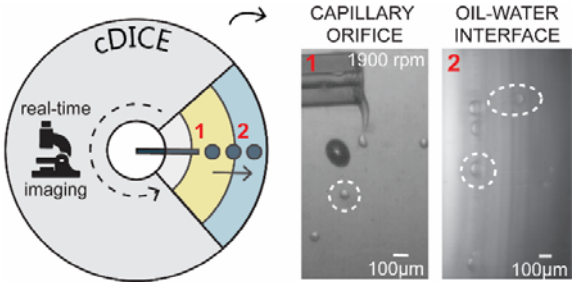

We developed a high-speed microscopy setup to study giant unilamellar vesicle formation in cDICE, revealing a complex droplet formation process occurring at the capillary orifice and size-selectivity at the oil-water interface.

Abstract (max 250 words)

Giant unilamellar vesicles (GUVs) are widely used as three-dimensional *in vitro* model membranes in biophysics and as cell-sized containers in bottom-up synthetic biology. Despite their ubiquitous use, there is no one-size-fits-all method for their production. Over the years, numerous methods have been developed to meet the demanding requirements of reproducibility, reliability, and high yield, while simultaneously achieving robust encapsulation. Emulsion-based methods are often praised for their apparent simplicity and good yields; hence, methods like continuous droplet interface crossing encapsulation (cDICE) that make use of this principle, have gained popularity in recent years. However, the underlying physical principles governing the formation of GUVs in cDICE and related methods remain poorly understood. To gain a deeper understanding of GUV formation in cDICE, we have developed a high-speed microscopy setup that allows us to visualize GUV formation in real-time. Our experiments reveal a complex droplet formation process occurring at the capillary orifice,

generating both larger droplets and, likely, GUV-sized satellite droplets. Based on our observations and theoretical modelling of the fluid dynamics within the system, we find that the transfer of these droplets through the oil-water interface exhibits a size-selectiveness toward GUV-sized droplets. Finally, we demonstrate that protein in the inner solution affects GUV formation by increasing the viscosity and altering lipid adsorption kinetics. These results will not only contribute to a better understanding of GUV formation processes in cDICE and, by extension, in emulsion-based methods in general, but ultimately also aid the development of more reliable and efficient methods for GUV production.

Introduction

The quest to understand and manipulate the building blocks of life, including the countless interacting molecules and biochemical reactions making up cellular life, is a major aim of biophysics and synthetic biology.[1] One key tool in these fields are giant unilamellar vesicles (GUVs) as cell-sized, lipid bilayer-enclosed reaction compartments.[2,3] Since their first description[4] in 1969, GUVs have proven to be a powerful and versatile tool as they can be directly observed using real-time microscopy and easily manipulated using biophysical tools, making them ideal *in vitro* model membrane systems.[3,5,6] More recently, GUVs have also been proposed as containers for a future synthetic cell[7–10] and as reaction containers for chemistry and more complex cargo carriers in drug delivery[11,12].

Despite the widespread research use of GUVs, there is still no one-size-fits-all method for their production. Over the years, numerous methods have been developed to meet the demanding requirements of reproducibility, reliability, and high yield, while simultaneously achieving robust encapsulation. Historically, swelling-based methods (natural swelling[4], electroformation[13–16], and gel-assisted swelling[17–20]) have been used extensively for studying the biophysical properties of membranes. However, these easy-to-implement, high-yield methods offer poor control over encapsulation efficiency and the stoichiometry of encapsulated molecules. Thus, they only offer limited compatibility with establishing complex reconstituted systems. Emulsion-based techniques (water-in-oil droplets crossing an oil-water interface using gravity, centrifugation, microfluidic devices, or microfluidic jetting[21–27]) on the other hand, offer more control over GUV content and for complex encapsulation experiments, emulsion-based methods have therefore gained popularity in recent years.

One method that particularly gained a lot of traction is called continuous droplet interface crossing encapsulate (cDICE).[28–34] In cDICE, aqueous droplets that are produced at a capillary orifice are

continuously forced through an oil-water interface by centrifugal force in a rotating chamber, thereby forming a lipid bilayer and thus GUVs.[28] Recent optimization has made the method compatible with a wide range of biological systems, thereby offering control over encapsulated content, a high GUV yield, and straightforward implementation.[29] However, our understanding to which degree the encapsulated contents' complexity in cDICE can be extended, with respect to both physical properties (*e.g.* viscosity of encapsulated fluid) and physicochemical properties (*e.g.* which proteins and protein systems), remains limited. While many successes have been celebrated using cDICE, we still do not understand the underlying GUV formation process and how this affects the inherent variability in content encapsulation and yield seen in cDICE.[10]

To gain a deeper understanding of GUV formation in cDICE, we have developed a high-speed microscopy setup that allows us to visualize the GUV formation process inside the rotating chamber in real-time. We focused on the capillary orifice, where initial droplet formation occurs, and on the oil-water interface, where droplets are converted into GUVs. Our experiments reveal a complex droplet formation process occurring at the capillary orifice, governing both the formation of larger droplets and, likely, GUV-sized satellite droplets. The transfer of these droplets through the oil-water interface appears to exhibit selectivity toward GUV-sized droplets. We support these observations with theoretical modelling of the fluid dynamics within the system. Finally, we demonstrate that the addition of protein to the inner solution increases the viscosity and alters the kinetics of lipid adsorption, thereby significantly influencing the process of GUV formation.

Results and discussion

Design of the cDICE imaging setup and general workflow

In order to gain a better understanding of GUV formation in cDICE, we developed a high-speed microscopy setup to visualize the process in real-time (Fig. 1). We designed the setup so that the camera is suspended vertically above the cDICE apparatus, capturing the light of a light source located directly beneath the rotating chamber (see method section for a full description of the setup; Fig. 1a). This way, we are able to capture the process along the horizontal axis of the rotational chamber: from the capillary orifice, where initial droplet formation occurs (Fig. 1b i), to the oil-water interface, where droplets are converted into GUVs (Fig. 1b ii).

Due to the high rotation speeds that are used in cDICE (~ 1900 rpm), all processes happen on a very fast timescale, on the order of milliseconds (10^{-6} - 10^{-5} s). To obtain a sufficiently high time resolution, we therefore used fast cameras in combination with brief exposure times up to 1 µs, reaching frame rates up to 30,000 fps.

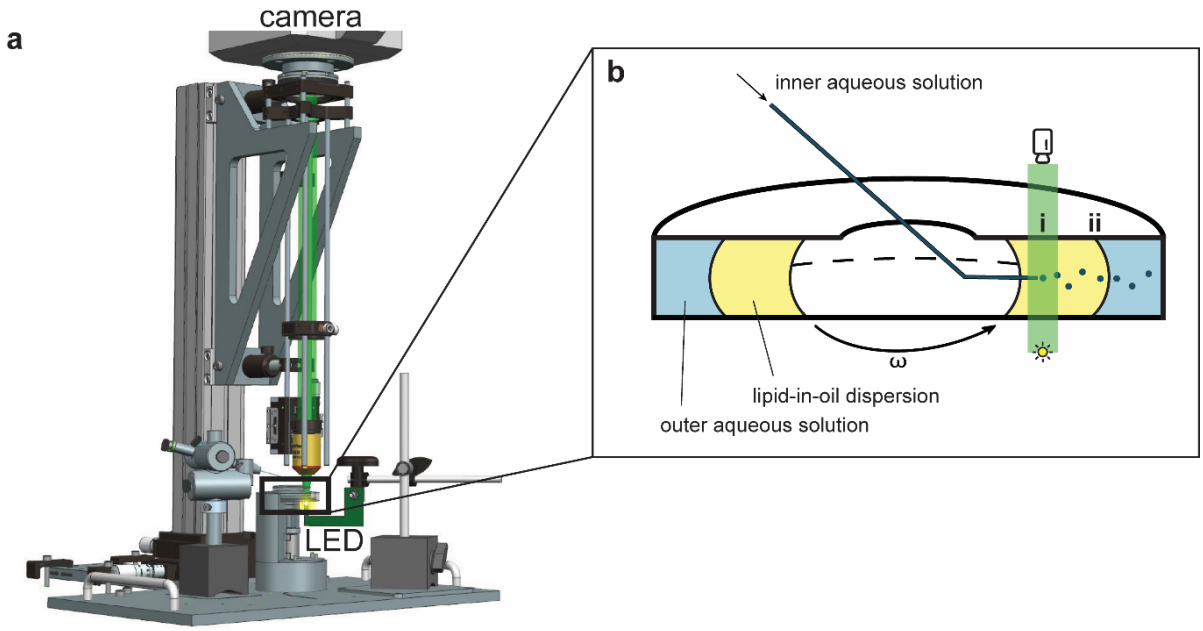

Figure 1. High-speed imaging setup to visualize GUV formation in cDICE. **a.** The imaging setup consists of a high-speed camera suspended above the rotating chamber and an intense light source located directly below the rotating chamber. **b.** In cDICE, (i) aqueous droplets are generated at the capillary orifice; subsequently travel outward through the lipid-in-oil dispersion; and finally (ii) traverse the oil-water interface, where droplets are converted into GUVs.

While it is possible, and needed, to tweak various operational parameters to encapsulate a particular (non-)biological system in cDICE, we chose to use the parameters established in a recent optimization study by Van de Cauter *et al.*[29] as our standard operating conditions for cDICE. Specifically, we used a 100 µm diameter capillary, a rotation speed of 1900 rpm, and a flow rate of 25 $\mu Lmin^{-1}$. For the lipid-in-oil dispersion, DOPC lipids were dispersed using chloroform and we encapsulated G-buffer, relevant for and widely used in actin research, or phosphate buffered saline (PBS), supplemented with 18.5 % v/v density gradient medium OptiPrep™ to achieve a density difference between the inner and outer aqueous solution.

Droplet formation at the capillary orifice is governed by shear forces

The initial stage of GUV formation in cDICE consists of the generation of droplets at the capillary orifice, which is inserted perpendicularly into the oil layer in the rotating chamber. Surprisingly, when imaging the capillary orifice at the default condition, it immediately became clear that droplet

formation under the chosen operating conditions is a non-uniform, highly dynamic process with an irregular breakup pattern of a liquid stream into individual droplets (Fig. 2a, SI Mov. 1). This contrasts with the common assumption that droplet generation is a straightforward and simple process in which droplets are created at the capillary orifice and, once they reach a critical size (around the size of GUVs), they are sheared off and travel outward. Instead of this distinct droplet formation at the capillary orifice, we observed a tail of fluid exiting and often also adhering to the capillary. At the end of this fluid tail, droplets were split off at a fast rate. Upon silanization of the capillary, we no longer observed the fluid tail adhering to the capillary, resulting in a more stable droplet breakup mechanism (SI Fig. 1). This can likely be explained by an increased surface hydrophobicity upon silanization when compared to the uncoated, cut end and default polyimide capillary coating surrounding the capillary, which results in less wetting of the capillary surfaces.

Consistent with an irregular break up mechanism, we observed a large inter-experiment variability (Fig. 2c) that we attribute to a number of factors, including irregular capillary orifices resulting from a suboptimal cutting procedure or from capillary deterioration over sustained use, differences in capillary insertion angle, and the occasionally-observed presence of an air pocket at the base of the capillary. Note that none of these factors were visible by eye, but required a dedicated imaging setup to distinguish. Additionally, we observed that the droplets did not immediately travel outward as expected, but rather initially exhibited an inward movement towards the center of the rotating chamber, before travelling outward. Default operating conditions, *i.e.* a rotation speed of 1900 rpm, yielded droplets with a mean diameter of (68.6 ± 2.8) µm, and resulting in the formation of approximately 2500 droplets per second.

To better understand the observed droplet breakup mechanisms, we then turned to modeling the fluid dynamics within the system (Fig. 2b). Our video recordings suggest that droplet breakup at the tip of the capillary is induced by viscous shear stresses. For a capillary of outer diameter D immersed in a fluid of dynamic viscosity μ, shear-induced droplet break up at the capillary orifice requires the capillary number Ca to be larger than 1. Ca is given by $Ca = \mu U/\gamma$, where γ is the interfacial tension between the dispersed and the continuous phase. The flow velocity U at the point of insertion of the capillary is $U = \Omega R_i$, where R_i is the distance between the capillary orifice and the center of rotation of the chamber and Ω is the rotation speed. With $R_i \sim 1\,cm$, $\Omega \sim 1000 - 2700\,rpm$, $\mu \sim 4 - 5\,10^{-3}\,kgm^{-1}s^{-1}$ and assuming an interfacial tension between the inner solution and the oil phase of $\gamma \sim 10^{-3} - 10^{-2}$ ([29]), we expect the capillary number to be between 0.5 and 10. This is consistent with our observation that droplets are indeed sheared off the capillary, indicating $Ca > 1$.

cDICE experiments require high angular velocities (> 1000 rpm), producing flow instabilities in the wake of the capillary which we expect to impact droplet formation. Indeed, the Reynolds number, characteristic of the flow around the capillary, $Re_D = \rho U D/\mu$, yields values in the range of $Re_D \sim 200 - 300$, with $\rho \sim 0.934\ g/mL$ the density of the lipid-in-oil dispersion. For $Re_D \geq 47$, periodic vortex shedding in the wake of a cylinder is expected[35], and for $Re_D \geq 150$, further three-dimensional instabilities are predicted[35], suggesting that the wake around the capillary will also affect droplet breakup. Indeed, we observe oscillations in droplet breakup, caused by the non-linear effects in the wake, and the inner solution adhering to the outer capillary surface.

In our previous study we found that using a capillary with a 100 µm diameter opening prevents clogging at the expense of control over GUV size[29], but our video recordings show that using such large capillary openings leads to unstable droplet dripping mechanisms. The use of smaller capillary openings, in the range of 2-25 µm, has been demonstrated by Abkarian *et al.*[28]. The smaller inner diameter of the capillary used in that study may have a twofold effect on the droplet size distribution. First, the total interfacial force resisting the breakup of the droplet directly depends on the size of the neck, which is effectively set by the dimension of the capillary opening. As the droplet pinches off when the viscous force on the droplet exceeds the surface tension force, this leads to smaller droplet sizes. Additionally, smaller capillaries lead to a smaller Reynolds number, as it is proportional to the capillary outer diameter, and the wake behind the capillary will not be as unstable as it would be with larger capillaries, possibly not unstable at all. Consequently, droplets are more likely to shear off at the tip of the capillary cleanly for smaller capillary diameters.

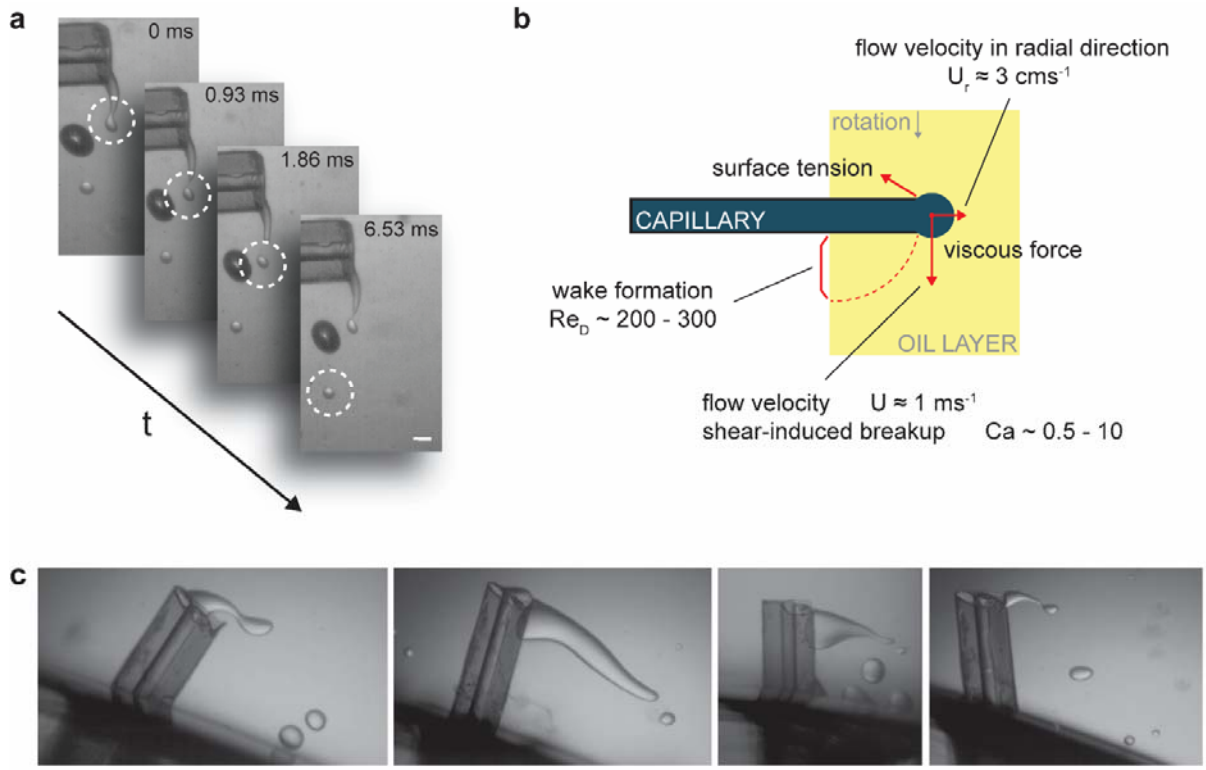

Figure 2. Droplet formation at the capillary orifice is governed by shear forces. **a.** Microscopic image sequence capturing a droplet of PBS buffer with 18.5 % v/v OptiPrep™ being sheared off from the liquid stream at the capillary orifice at a rotation speed of 1900 rpm. Scale bar indicates 100 µm. **b.** Illustration depicting the different forces acting at the capillary orifice: the capillary number Ca (Ca ~ 0.5-10) indicates a shear-induced breakup mechanism, while the Reynolds number (Re_D ~ 200-300) describes the wake formation behind the capillary. The shear velocity ($U \approx 1$ ms^{-1}) is larger than the flow velocity in the radial direction ($U \approx 3$ cms^{-1}), further indicating droplet formation is shear-induced. **c.** Representative field-of-views highlighting the high inter-experiment variability. Noticeable differences can be seen, *e.g.* in liquid stream, capillary orifice, and insertion angle. The capillary opening is 100 µm in all cases.

For larger capillary diameters, the formation of droplets in cDICE bears some similarities with the formation of droplets at T-junctions in microfluidics, a well-studied phenomenon.[36,37] In such microfluidic channels, the geometric confinement provided by the channels leads to flow restrictions on the continuous phase at the origin of a squeezing pressure. This pressure promotes droplet break up at much smaller values of Ca as compared to our experiments. However, there are similarities in the droplet formation regimes. For example, a decrease in droplet volume for increasing values of Ca has been widely reported.[36,37] These studies have also reported a transition from a breakup droplet

formation mechanism for low values of Ca to a dripping mechanism at higher Ca, whereby a long thread of the dispersed phase forms and droplets pinch off at the end of the thread.

Droplet size is proportional to the rotation speed

To explore factors that influence droplet break-off in cDICE, we next altered the rotation speed of the rotating chamber. As the rotation speed of the chamber increases, the flow velocity at the capillary orifice also increases and the viscous forces become stronger. This leads to the droplets being more likely to break up, resulting in smaller droplets. In line with this expectation, an increase in rotation speed to 2700 rpm resulted in smaller droplets formed at a higher frequency ((28.5 ± 8.7) µm and ~34,500 droplets per second; Fig. 3, SI Mov. 2). Decreasing the rotation speed to 1000 rpm, the lowest speed at which oil and water layers are stably separated and GUVs can be produced, had the opposite effect, *i.e.* leading to larger droplets formed at a lower frequency ((273 ± 41) µm and ~40 droplets per second; Fig. 3, SI Mov. 3). Even at these lower speeds, the flow around the droplets forming at the tip of the capillary of radius a_o, is dominated by the shear component of the velocity field due to the rotation of the chamber. Indeed, the flow velocity due to the chamber rotation is large, $U \approx \Omega R_i \approx 1ms^{-1}$. The velocity in the radial direction can be inferred from a scaling between the centrifugal forces and viscous forces. This scaling yields $U_r = (\rho_i - \rho_o){a_o}^2\Omega^2 R_i/\mu$, where ρ_i is the density of the inner solution and ρ_o the density of the outer solution. Given that $(\rho_i - \rho_o) \sim 30kgm^{-3}$, this yields $U_r \approx 3cms^{-1}$ and is negligible compared to the shear velocity. Droplet formation is thus shear-induced in a broad range of rotation speeds, encompassing both lower and higher speeds than the default of 1900 rpm.

While a rotation speed of 1900 rpm resulted in the narrowest droplet size distribution of all explored rotation speeds, interestingly, a rotation speed of 1000 rpm resulted in two distinct populations. One primary population of droplets with a mean diameter of (273 ± 41) µm and a secondary population consisting of smaller droplets with a mean diameter of (15.9 ± 7.3) µm. Occasionally, droplet formation was disrupted when *e.g.* a droplet merged with the liquid stream or collided with the capillary. The observed population of small droplets are satellite droplets and are produced when a bigger droplet breaks off from the main liquid thread at the tip of the capillary (SI Mov. 3). Such satellite droplets have previously been observed in many breakup configurations, from T-junctions to the breakup of droplets in pure shear.[38] Note that while we did not observe any satellite formation for rotation speeds > 1000 rpm, this may be due to our limited optical and temporal resolution. Droplets with a diameter ~15 µm were at the limits of our image resolution, droplets of any smaller diameter were too small to be identified and measured with sufficient certainty. The large pixel size ((2.431 ± 0.105) µm) in comparison to the droplet size characterized, in combination with a

measurement error of 2 µm, calculated from measuring a subset of data in triplicate, posed a limit on our analysis. Additionally, the high speed of the process, resulting in motion blur and droplets quickly moving out of focus, as well as the limited contrast, caused by the small difference in refractive index between the droplets and the surrounding medium (1.333 for water *vs* 1.403 for silicone oil), makes it difficult to distinguish the droplets from the background in the video recordings.

In addition to the small satellite droplets we observed at 1000 rpm, smaller droplets could theoretically also be formed when larger droplets break up due to shear forces generated in the flow by the rapid relative motion of the bottom wall of the rotational chamber with respect to the capillary. In the oil layer, the characteristic shear rate $\dot{\varepsilon}$ scales with $\dot{\varepsilon} \sim \Omega R_i/h$, where h is the vertical distance from the capillary to the bottom of the flow chamber. One can define another capillary number as $Ca_{\dot{\varepsilon}} = \mu \dot{\varepsilon} a/\gamma$, where a is the radius of the droplet.[39,40] This number characterizes the relative magnitude of the viscous shear forces due to the shear rate $\dot{\varepsilon}$ and the surface tension forces. $Ca_{\dot{\varepsilon}} = 1$ corresponds to a condition where the smallest droplets cannot be further broken up by the shear[39,40] and yields $a \sim \gamma/\mu\dot{\varepsilon}$. Knowing $h \sim 0.5\,cm$, we find that the interfacial tension of the monolayer at the inner solution/oil interface needs to be approximately $\gamma \sim 10^{-6}\ Nm^{-1}$ to produce droplets of $a \sim 5\ \mu m$, equivalent to the final GUV size. This value for an interfacial tension at an aqueous/oil interface is extremely low and not expected, even in presence of surfactants or lipids. Hence, we conclude that it is unlikely GUV-sized droplets form by shear force induced droplet breakup after droplet formation at the capillary orifice.

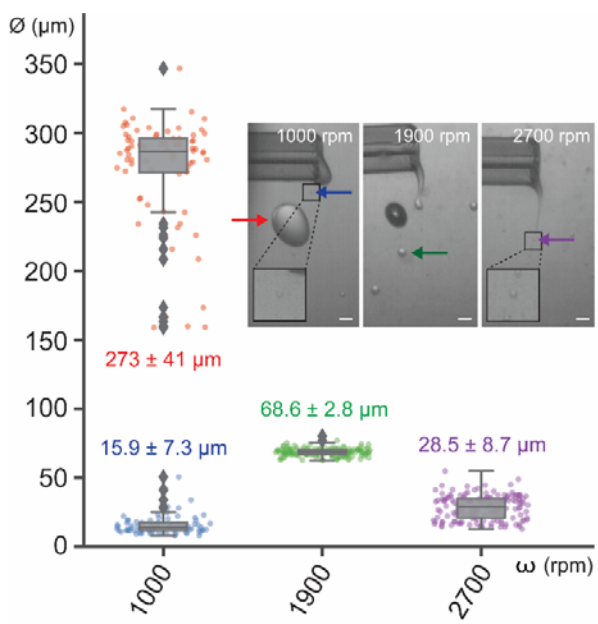

Figure 3. Size distributions of droplets for different rotation speeds. (single column)

Boxplots of droplet diameter at rotation speeds of 1000 rpm, 1900 rpm, and 2700 rpm (n = 148, 152, and 157, respectively, for N=1). Individual data points indicate single droplets and boxplots indicate medians and quartiles, while outliers are marked with individual diamond shapes. A rotation speed of 1000 rpm resulted in two distinct droplet populations: large droplets of mean size (273 ± 41) µm (red) and satellite droplets of mean size (15.9 ± 7.3) µm (blue). A rotation speed of 1900 rpm resulted in the narrowest distribution, with a mean droplet size of (68.6 ± 2.8) µm (green). 2700 rpm resulted in the smallest droplet sizes, with a mean size of (28.5 ± 8.7) µm (purple). Inset: representative field-of-views for the different rotation speeds indicating the formed droplets with arrows. Scale bars indicate 100 µm.

Droplet formation in cDICE occurs on extremely short timescales; for the default conditions (*i.e.* 1900 rpm, 25 uLmin^{-1}) we observed droplets of approximately ~70 µm in diameter being sheared off at a frequency of ~2500 Hz. Theoretically, given a total encapsulation volume of 100 µL, > 500.000 droplets are formed during a single experiment. Interestingly, these numbers do not correspond to the final number of GUVs produced using cDICE, as reported in other publications (~ 1000 GUVs[29]). Furthermore, it is worth nothing that the sizes of the droplets observed in the imaging experiments (*i.e.* ~70 µm for the default conditions) are an order of magnitude larger than the size distributions for GUVs generally obtained using cDICE. These discrepancies indicate a sub-optimal GUV formation process downstream whereby most droplets do not convert into GUVs at the oil-water interface.

Protein in the inner solution affects viscosity and lipid adsorption

Next, we set out to study the effect of proteins on droplet formation at the capillary orifice. It is well known that encapsulation of more complex solute mixtures, such as proteins and their associated buffers, leads to a decreased yield and variable encapsulation efficiencies[29,41]. For cDICE specifically, it has been reported that the yield decreased at high protein concentration[42], yet no more extensive analysis has been done so far. We chose to investigate the effects of actin and tubulin, due to the widespread efforts for cytoskeletal reconstitution inside GUVs.

Upon addition of either protein, droplet breakup at the capillary orifice occurred in the same fashion, *i.e.* droplets were sheared off a liquid stream exiting the capillary. However, the previously observed oscillations of the liquid stream appeared dampened (Fig. 4a). Remarkably, in the case of tubulin, the liquid stream displayed a tendency to adhere to the air-oil interface. To explain these observations, we characterized the inner solution. We looked into both the physical properties, *i.e.* dynamic

viscosity as determined by bulk shear rheology, and physicochemical properties, specifically lipid adsorption rate determined from pendant drop tensiometry.

In presence of actin and tubulin, the dynamic viscosity increased with respect to its accompanying buffer, G-buffer and MRB80 buffer respectively (Fig. 4c). For actin (1 µM in G-buffer, 6.5 % v/v OptiPrep™), an almost threefold increase from 1.58 cP to 4.61 cP was observed (Fig. 4c, yellow bar), while for tubulin (33.33 µM in MRB80 buffer, 1.75 % w/v sucrose), the viscosity increased fourfold from 1.57 cP to 6.49 cP (Fig. 4c, red bar). All solutions still exhibited Newtonian fluid behaviour. Important to note is that the used concentrations of added proteins remain within the micromolar range and are widely used in the field. Interestingly, the viscosity of the inner solution containing protein was similar to the viscosity of the continuous phase, *i.e.* the surrounding lipid-in-oil dispersion (Fig. 4c, 'LOD' bar). This similarity could explain the reduced instability and turbulence observed when imaging the capillary orifice. Moreover, the greater viscosity of the inner solution with protein could lead to a more consistent droplet breakup, potentially hampering satellite droplet formation. Altogether, these results show a nuanced interplay between the physical properties of the encapsulation solution, varying with its composition (even at low protein concentrations), and the fluid dynamic processes that govern droplet breakup.

To investigate how the addition of protein to the inner solution alters the physicochemical properties of the interface, we used pendant drop tensiometry[43] to study lipid monolayer formation in a controlled environment. We analyzed the lipid adsorption kinetics and interfacial tension dynamics of the water-oil interface for different encapsulation solutions, mimicking droplet formation at the capillary orifice. It has been shown that proteins spontaneously adsorb at the oil-water interface and their behaviour cannot unequivocally be attributed to a single protein property, with thermodynamic stability, structural properties, and concentration all being contributing factors.[44,45] Particularly, actin has been shown to exhibit surface activity in a charge-dependent manner, influenced by both lipid and buffer composition, with a more pronounced effect observed for the filamentous form compared to actin monomers.[46–48]

Upon adding 4 µM actin to the inner solution, a pronounced decline in interfacial tension was observed (Fig. 4b, purple curve), with some droplets detaching before the end of the experiment (Fig. 4b, dashed lines). This trend was consistent for tubulin (Fig. 4b, green curve). To examine the roles of actin and tubulin as surface-active agents in the interfacial tension, we then compared the interfacial tension dynamics against a lipid-free oil dispersion. Both actin and tubulin had only a marginal impact on interfacial tension when compared to the protein-free condition (Fig. 4b, black curve *vs* purple

curve and grey curve *vs* green curve). Interestingly, while actin and lipids individually at the interface exhibited slow kinetics, their combined presence displayed an accelerated decrease (Fig.4b, yellow curve), suggesting a synergistic effect beyond mere additivity. We found this effect could not be countered via electrostatic or steric repulsion (*i.e.* presence of charged or PEGylated lipids, respectively, SI Fig. 2). These results imply that actin could, for example, quickly cover the surface of the droplets traversing the lipid-in-oil dispersion, potentially impeding lipid monolayer formation and/or monolayer zipping. However, the full extent of this synergistic effect is yet to be uncovered. Furthermore, these results underscore the importance of the compositions of both inner solution and lipid-in-oil dispersion, as both affect mono- and bilayer formation.

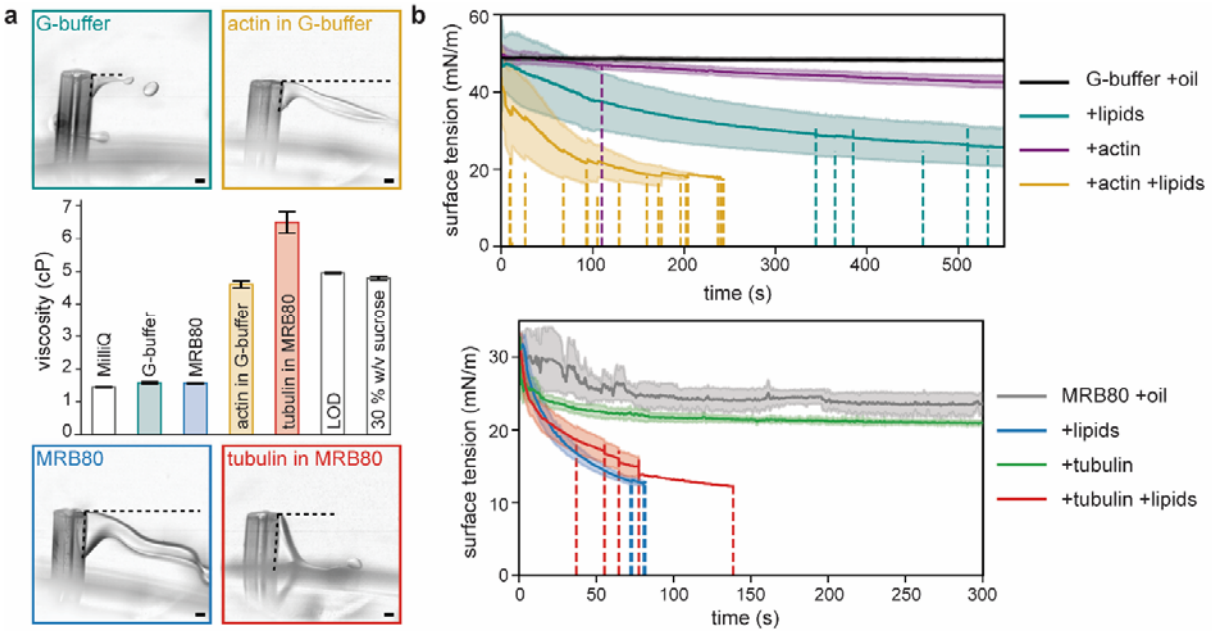

Figure 4. Effect of protein on aqueous solution properties.

a. Representative field-of-views of droplet formation at the capillary orifice for different protein solutions. Horizontal dotted lines indicate the tail length just before the drop breaks off, while vertical dotted lines along the capillary indicate the extent of external capillary surface wetted by the aqueous solution. Images are background subtracted for better contrast. Scale bars indicate 100 µm. Middle: Dynamic viscosity measured using a parallel plate rheometer for different buffers (G-buffer with 6.5 % v/v OptiPrep™, MRB80 with 1.75 % w/v sucrose) and protein solutions (actin and tubulin), along with water (MilliQ), lipid-in-oil dispersion (LOD) and 30 % w/v sucrose solution in MRB80 for reference. Error bars represent standard deviation. **b.** Interfacial tension kinetics measured using pendant-drop tensiometry for different combinations of aqueous and oil solutions; G-buffer and actin (top), and MRB80 and tubulin (bottom). Solid lines

represent the average values and the shaded region corresponds to standard deviation. The vertical dotted lines represent the event of falling of a drop and truncation of data.

GUV formation at the oil-water interface seems size selective

The discrepancy between the size and number of droplets forming at the capillary orifice and the GUVs found in the outer aqueous solution, points to hidden mechanisms generating smaller droplets than those observed plus the loss of a substantial fraction of droplets that are not converted into GUVs. As mentioned above**,** one possible explanation is that GUVs are instead formed from small satellite droplets that are produced when bigger droplets break off from the main liquid thread at the tip of the capillary. However, due to our resolution limit, we were not able to observe these in conditions > 1000 rpm. Therefore, we imaged the oil-water interface where the final step of GUV formation in cDICE occurs: droplets transfer through the oil-water interface and two monolayers fuse together to form a bilayer (Fig. 5a). As postulated by Abkarian *et al.*[28], the two monolayers can also form a pore, thereby causing the droplet to burst, resulting in no GUV being formed.

In our experiments, we did not observe a clear transfer of droplets through the interface nor bursting of droplets, possibly because resolving GUV-sized droplets at the interface was not feasible with the limited imaging contrast of standard bright field illumination. Instead, we made two striking observations.

First, we observed droplets several orders of magnitude larger than the typical size of GUVs which were stationary on the oil-water interface (Fig. 5b, SI Mov. 4). The stationary droplets showed a decreased contrast on the side of the outer aqueous phase, suggesting partial transfer across the interface. Abkarian *et al.*[28] described a formula for calculating the flight time of the droplet, *i.e.* the transfer time to the oil-water interface, which should be longer than the typical time needed for lipids to fully coat the droplet surface and thus allow successful GUV production. Since the transfer time is inversely proportional to the radius of the droplets squared, it is possible that the flight time of these larger droplets is too short for lipids to fully adsorb on the interface. Consequently, no zipping mechanism is possible, leading to these larger droplets crowding the interface, as we observed in our video recordings.

A second observation was the formation of comet tails (Fig. 5c): droplets that did pass the interface dragged a tail of the oil solution into the outer aqueous solution, likely because the oil did not drain quickly enough and thus prevented monolayer fusion. Due to the difference in contrast with the outer aqueous phase, we infer that oil is still present between the part of the interface dragged into

the outer phase and the droplet. The Bond number $Bo = \frac{\Delta\rho a r^2}{\gamma}$, where a is the acceleration and r the radius of droplet, represents the ratio of centrifugal force to surface tension force. For these large droplets, Bo is on the order of 1, meaning they will deform the interface, as observed in our video recordings, and drag the oil phase into the outer aqueous phase. This results in the observed comet tail formation and no GUV formation from the droplets undergoing this process.

As we find that the addition of protein to our inner solution significantly alters the characteristics of the solution and affects droplet formation at the capillary orifice, we asked how the increased viscosity and altered lipid adsorption kinetics might impact the transfer of droplets through the oil-water interface. The accelerated lipid adsorption due to the addition of protein does not lead to a decreased flight time of the droplets, thereby not adversely affecting droplet transfer or monolayer zipping. On the other hand, the increased viscosity of the inner solution could influence the timescale of the drainage of the lubrication film, *i.e.* the lipid-in-oil dispersion in between the droplet and the oil-water interface, required for successful monolayer zipping. Furthermore, the increased viscosity could reduce the flow caused by Marangoni stresses, which play a role in facilitating the zipping process.[28]

An approximate breakthrough condition for spherical objects of radius a to pass through an interface of interfacial tension γ is $(\rho_i - \rho_o)\Omega^2 R_o a^2/\gamma \geq 3/2$, where R_o is the distance between the axis of rotation and the location of the oil-outer solution interface.[49] For small droplets of radius $a \sim 5\mu m$ to cross the interface, a low surface tension on the order of $\gamma \sim 10^{-6} Nm^{-1}$ is required. Such low surface tension has been reported for lipid bilayers[50] and therefore if such small droplets are present in the oil phase, they can cross the interface to form GUVs. It should be emphasized that the breakthrough condition sets a criterion for the smallest droplet that can cross the interface. Any droplet larger than 10 μm in diameter would be expected to cross the interface as well and form larger GUVs. However, this is at odds with the observed distribution of GUV radii as well as the observations of large droplets at the oil-water interface.

Comparing those GUV size distributions obtained with cDICE with those obtained by eDICE, a recent adaptation of cDICE where the droplets are generated by emulsifications (using vortexing, pipetting, or scraping) instead of via the capillary, we noticed a similar general trend: the final GUV size distribution was similar for the two methods[51], despite the size distribution of the droplets looking vastly different (SI Fig. 3). Furthermore, we found GUV sizes to be remarkably similar for different membrane compositions in eDICE (SI Fig. 4). Taken together, these cDICE and eDICE results indicate a

yet unknown mechanism for size-selectiveness at the oil-water interface that promotes the production of similarly-sized GUVs for a wide distribution of droplet sizes. For example, it is possible that GUVs form at the oil-water interface in cDICE and eDICE by pinching off from larger droplets sitting at the interface. While we did not observe any event like this, we would expect this process to happen on a length scale (and possible time scale) beyond the resolution of our imaging setup.

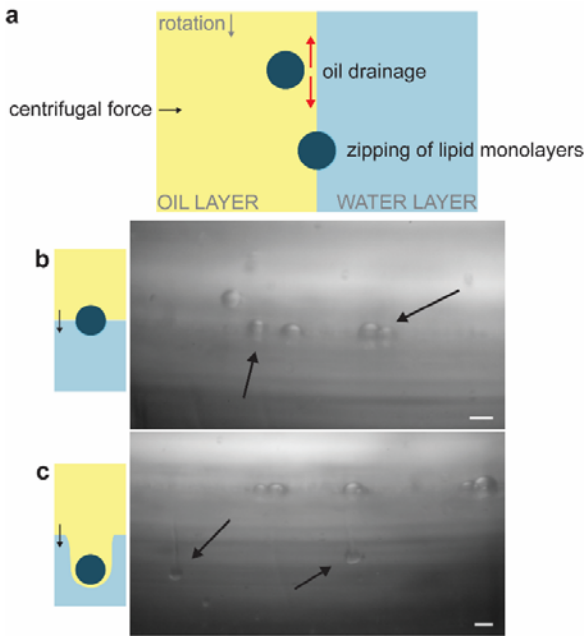

Figure 5. Droplet transfer through the oil-water interface is suboptimal. (single column)

a. The lipid-in-oil dispersion in between the approaching lipid monolayer-covered droplets and the oil-water interface needs to be drained for the two monolayers to zip together and successful GUV formation to occur. **b.** When droplets are not fully covered by a lipid monolayer when reaching the oil-water interface, successful transfer cannot occur and instead, stationary, semi-transferred droplets are observed. Scale bar indicates 100 µm. **c.** When drainage of the oil layer between the approaching droplet and oil-water interface is insufficient, the formation of comet tails can be observed: a droplet distorts the oil-water interface and drags the lipid-in-oil dispersion into the outer aqueous solution, hindering successful GUV formation. The Scale bar indicates 100 µm.

Conclusion

In summary, by visualizing droplet formation and droplet interface transfer in cDICE in real time, we were able to gain a deeper understanding of the underlying mechanisms governing GUV formation. We found that droplet formation at the capillary orifice, contrary to common belief, produced droplets that are much larger than the size of the final GUVs. Only as a side process, smaller satellite

444 droplets are being formed. Even smaller droplets, including GUV-sized droplets, could not be
445 resolved due to the limited resolution of our setup. Furthermore, we showed that the addition of
446 protein to the inner solution increases its viscosity and changes interfacial tension dynamics, both
447 directly impacting droplet formation and interface transfer. Imaging of the oil-water interface
448 revealed that droplet transfer is frequently stalled, sub-optimal for large droplets, and exhibits a size-
449 selectivity. This size-selectivity of droplet transfer to GUVs was further confirmed using eDICE, a
450 variant of cDICE where no capillary is used, which yielded similar size distribution despite vastly
451 different droplets as input. Further studies are needed to further elucidate the effect of lipid
452 composition, including cholesterol or charged lipids, and different proteins or protein mixes. We
453 believe the presented results can be of interest not only for cDICE but to other emulsion-based GUV
454 formation methods as well, ultimately contributing to the development of more reliable and efficient
455 methods for GUV production. Our study furthermore emphasizes the need for inter-disciplinary
456 collaboration to fully grasp the intricacies of the processes involved in emulsion-based GUV
457 production methods. Altogether, this research is just a prologue to a larger narrative and we hope it
458 will serve as a stepping stone for future research, enhancing emulsion-based GUV formation along
459 the way.
460

461 **Methods**

462 *Design and fabrication of the spinning device*

463 The cDICE device was identical to Van de Cauter *et al.*[29]. An additional opening underneath the
464 spinning chamber was created by removing part of the motor housing. This way, the light source
465 could be placed directly below the spinning chamber to achieve transillumination. The design for the
466 adjusted cDICE device is available on GitHub (https://github.com/GanzingerLab).
467

468 *Fabrication of spinning chambers*

469 Transparent, cylindrical chambers, 35 mm in diameter and 10 mm in height, were made from two
470 lids of Petri dishes (Falcon® REF 351008). To create a waterproof, closed chamber, the sides of the
471 two lids were first sanded using sandpaper to create a rough surface after which they were glued
472 together using a thin layer of optical glue (Norland Optical Adhesive 81). After curing of the glue
473 using UV light, the side of the chamber was wrapped with a strip of Parafilm®. The chambers include
474 a circular opening of 15 mm in diameter in the top to allow facile access to the solutions with the
475 capillary.
476

477 *General cDICE experimental workflow*

The general cDICE experimental workflow and preparation of lipid-in-oil dispersion was based on Van de Cauter *et al.*[29]. The following parameters differed: The volume of the outer solution was increased to 1.07 mL to account for the difference in dimensions between the 3D printed spinning chambers, as used in Van de Cauter *et al.*[29], and the Petri dish spinning chambers that were used for imaging experiments, as mentioned above. Room humidity was not controlled during imaging experiments and the chambers were spun for the entirety of the imaging experiments instead of a predetermined time. G-buffer (5 mM tris(hydroxymethyl)aminomethane hydrochloride (Tris-HCl) pH 7.8 and 0.1 mM calcium chloride ($CaCl_2$), 0.02 mM adenosine triphosphate (ATP) and 4 mM dithiothreitol (DTT)) with 18.5 % v/v OptiPrep™ was encapsulated in every experiment, unless specified otherwise.

Home-built imaging setup

The light of a single LED (Luxeon V2, 315lm@700mA; used without lens) or a Lumencor light engine (SOLA 6-LCR-SB) was collected by a 200 mm focal length achromatic lens (Thorlabs AC254-200-A-ML; lens mount: Thorlabs CXY1). The setup was equipped with a 4X or 10X objective (Nikon Plan Fluor 4x/0.13 PhL DL and Nikon Plan Fluor 10x/0.30 ∞/0.17 WD 16, respectively) that was mounted on a Z-stage (Thorlabs CT1; adapter: Thorlabs SM1A10). X/Y motion control was provided by two translational stages with a step size of 25 mm (Thorlabs PT1). Images were recorded using a high-speed camera (Kron Technologies Chronos 2.1-HD and Photron FASTCAM SA4) which was mounted on the setup using a custom-designed 3D printed construction. The full setup was mounted on a Thorlabs cage system that was mounted on a breadboard (Thorlabs MB1030/M) to easily move the full setup over the cDICE device. The full component list and design plans can be found on GitHub (https://github.com/GanzingerLab).

Droplet size analysis

Droplet size analysis was performed manually using the Fiji software[52]. The image pixel size was derived from three independent measurements of the capillary opening, accounting for capillary size uncertainty. Triplicate measurements were performed for a subset of each dataset to quantify the measurement error. For each droplet, we then measured both area and diameter, yielding two independent measurements of the droplet diameter with associated error calculated through error propagation. Data visualization was achieved through Python-generated plots. The frequency was estimated using the mean droplet size and the flow rate of the inner solution. Note that for the analysis of droplet size and frequency, we used video recordings in which the fluid tail did not adhere to the capillary surface (one experiment per condition).

Viscosity measurements

The dynamic viscosities of the solutions were measured on a Kinexus Malvern Pro rheometer. A stainless steel plate-plate geometry with 40 and 20 mm radius were used for buffer solutions and protein-containing solutions respectively. Viscosity was measured every 5 seconds as a function of shear rate with a 2 min logarithmic viscometry ramp from 0.5 s^{-1} to 100 s^{-1}. As expected for simple viscous liquid, viscosities for higher shear rate were constant. The values at 100 s^{-1} were used to calculate the reported viscosity of each solution. MRB80 buffers consists of 80 mM piperazine-N,N′-bis(2-ethanesulfonic acid) (PIPES) pH 6.8, 4 mM magnesium chloride ($MgCl_2$), and 1 mM ethylene glycol-bis(β-aminoethyl ether)-N,N,N′,N′-tetraacetic acid (EGTA).

Tensiometry measurements

The pendant drop measurements were performed using a DSA 30S drop shape analyser (Kruss, Germany) and analysed with the Kruss Advanced software. Experimental conditions for G-buffer and actin-containing solutions were as described in Van de Cauter *et al.*[29], while changes for MRB80 buffer and tubulin-containing solutions are described below. Initially a 2 µL droplet of aqueous solution is drawn in a lipid-in-oil dispersion containing glass cuvette (Hellma Analytics) and then volume of the droplet is adjusted to 8 µL using an automated dosing system from a hanging glass syringe with needle diameter of 0.313 mm (Hamilton). As soon as the droplet reached its final volume, droplet was analysed (for 300 seconds at 25 fps for solutions containing tubulin and lipids and at 5 fps for rest of the solutions) by automatic contour detection and fitted with the Young-Laplace equation to yield the interfacial tension. The surface tension values are smoothened with a rolling-mean of 1 sec. Room humidity was not controlled. In several experiments, interfacial tension decreased very rapidly (abnormally), causing the droplet to detach as soon as they are formed. These measurements were discarded from analysis.

Acknowledgements

We thank Roy Hoitink for his contributions during the initial exploration of the imaging setup, SaFyre Reese for experimental help during parameter screening, and Irene Istúriz Petitjean for help with rheology experiments. We would also like to thank Dr. Arjen Jakobi for generously lending us the Chronos 2.1-HD camera. We acknowledge financial support by the “BaSyC – Building a Synthetic Cell” Gravitation grant (024.003.019) of The Netherlands Ministry of Education, Culture and Science (OCW) and The Netherlands Organization for Scientific Research (NWO) (M.D. and G.H.K.) and NWO-WISE funding (K.A.G.). Part of this research was funded by a Pieter Langerhausen Stipendium of the Koninklijke Hollandsche Maatschappij der Wetenschappen (K.A.G).

References

(1) Ganzinger, K. A.; Schwille, P. More from Less – Bottom-up Reconstitution of Cell Biology. *Journal of Cell Science* **2019**, 11.
(2) Walde, P.; Cosentino, K.; Engel, H.; Stano, P. Giant Vesicles: Preparations and Applications. *Chem. Eur. J. of Chem. Bio.* **2010**, *11* (7), 848–865. https://doi.org/10.1002/cbic.201000010.
(3) Dimova, R.; Marques, C. M. *The Giant Vesicle Book*, 1st ed.; CRC Press, 2019.
(4) Reeves, J. P.; Dowben, R. M. Formation and Properties of Thin-Walled Phospholipid Vesicles. *J. Cell. Physiol.* **1969**, *73* (1), 49–60. https://doi.org/10.1002/jcp.1040730108.
(5) Dimova, R. Giant Vesicles and Their Use in Assays for Assessing Membrane Phase State, Curvature, Mechanics, and Electrical Properties. *Annu. Rev. Biophys.* **2019**, *48* (1), 93–119. https://doi.org/10.1146/annurev-biophys-052118-115342.
(6) Papahadjopoulos, D.; Kimelberg, H. K. Phospholipid Vesicles (Liposomes) as Models for Biological Membranes: Their Properties and Interactions with Cholesterol and Proteins. *Progress in Surface Science* **1974**, *4* (C), 141–144, IN9, 145–232. https://doi.org/10.1016/S0079-6816(74)80006-7.
(7) *BaSyC - Building a Synthetic Cell*. BaSyC. https://www.basyc.nl/ (accessed 2020-11-23).
(8) Mulla, Y.; Aufderhorst-Roberts, A.; Koenderink, G. H. Shaping up Synthetic Cells. *Phys. Biol.* **2018**, *15* (4), 041001. https://doi.org/10.1088/1478-3975/aab923.
(9) Gaut, N. J.; Adamala, K. P. Reconstituting Natural Cell Elements in Synthetic Cells. *Advanced Biology* **2021**, *5* (3), 2000188. https://doi.org/10.1002/adbi.202000188.
(10) Van de Cauter, L.; van Buren, L.; Koenderink, G. H.; Ganzinger, K. A. Exploring Giant Unilamellar Vesicle Production for Artificial Cells – Current Challenges and Future Directions. *Small Methods n/a* (n/a), 2300416. https://doi.org/10.1002/smtd.202300416.
(11) Sercombe, L.; Veerati, T.; Moheimani, F.; Wu, S. Y.; Sood, A. K.; Hua, S. Advances and Challenges of Liposome Assisted Drug Delivery. *Front. Pharmacol.* **2015**, *6*. https://doi.org/10.3389/fphar.2015.00286.
(12) Allen, T. M.; Cullis, P. R. Liposomal Drug Delivery Systems: From Concept to Clinical Applications. *Advanced Drug Delivery Reviews* **2013**, *65* (1), 36–48. https://doi.org/10.1016/j.addr.2012.09.037.
(13) Angelova, M. I.; Dimitrov, D. S. Liposome Electroformation. *Faraday Discussions of the Chemical Society* **1986**, *81*, 303–311. https://doi.org/10.1039/DC9868100303.
(14) Montes, L.-R.; Alonso, A.; Goñi, F. M.; Bagatolli, L. A. Giant Unilamellar Vesicles Electroformed from Native Membranes and Organic Lipid Mixtures under Physiological Conditions. *Biophysical Journal* **2007**, *93* (10), 3548–3554. https://doi.org/10.1529/biophysj.107.116228.
(15) Breton, M.; Amirkavei, M.; Mir, L. M. Optimization of the Electroformation of Giant Unilamellar Vesicles (GUVs) with Unsaturated Phospholipids. *J Membrane Biol* **2015**, *248* (5), 827–835. https://doi.org/10.1007/s00232-015-9828-3.
(16) Dimova, R.; Aranda, S.; Bezlyepkina, N.; Nikolov, V.; Riske, K. A.; Lipowsky, R. A Practical Guide to Giant Vesicles. Probing the Membrane Nanoregime via Optical Microscopy. *Journal of Physics Condensed Matter* **2006**, *18* (28), S1151–S1176. https://doi.org/10.1088/0953-8984/18/28/S04.
(17) Horger, K. S.; Estes, D. J.; Capone, R.; Mayer, M. Films of Agarose Enable Rapid Formation of Giant Liposomes in Solutions of Physiologic Ionic Strength. *J. Am. Chem. Soc.* **2009**, *131* (5), 1810–1819. https://doi.org/10.1021/ja805625u.
(18) Weinberger, A.; Tsai, F.-C.; Koenderink, G. H.; Schmidt, T. F.; Itri, R.; Meier, W.; Schmatko, T.; Schröder, A.; Marques, C. Gel-Assisted Formation of Giant Unilamellar Vesicles. *Biophysical Journal* **2012**, *105* (1), 154–164. https://doi.org/10.1016/j.bpj.2013.05.024.
(19) López Mora, N.; Hansen, J. S.; Gao, Y.; Ronald, A. A.; Kieltyka, R.; Malmstadt, N.; Kros, A. Preparation of Size Tunable Giant Vesicles from Cross-Linked Dextran(Ethylene Glycol) Hydrogels. *Chem. Commun.* **2014**, *50* (16), 1953–1955. https://doi.org/10.1039/C3CC49144G.
(20) Schultze, J.; Vagias, A.; Ye, L.; Prantl, E.; Breising, V.; Best, A.; Koynov, K.; Marques, C. M.; Butt, H.-J. Preparation of Monodisperse Giant Unilamellar Anchored Vesicles Using Micropatterned Hydrogel Substrates. *ACS Omega* **2019**, *4* (5), 9393–9399. https://doi.org/10.1021/acsomega.9b00912.

(21) Hu, P. C.; Li, S.; Malmstadt, N. Microfluidic Fabrication of Asymmetric Giant Lipid Vesicles. *ACS Applied Materials and Interfaces* **2011**, *3* (5), 1434–1440. https://doi.org/10.1021/am101191d.
(22) Ito, H.; Yamanaka, T.; Kato, S.; Hamada, T.; Takagi, M.; Ichikawa, M.; Yoshikawa, K. Dynamical Formation of Lipid Bilayer Vesicles from Lipid-Coated Droplets across a Planar Monolayer at an Oil/Water Interface. *Soft Matter* **2013**, *9* (40), 9539–9547. https://doi.org/10.1039/c3sm51766g.
(23) van Swaay, D.; deMello, A. Microfluidic Methods for Forming Liposomes. *Lab Chip* **2013**, *13* (5), 752. https://doi.org/10.1039/c2lc41121k.
(24) Funakoshi, K.; Suzuki, H.; Takeuchi, S. Formation of Giant Lipid Vesiclelike Compartments from a Planar Lipid Membrane by a Pulsed Jet Flow. *Journal of the American Chemical Society* **2007**, *129* (42), 12608–12609. https://doi.org/10.1021/ja074029f.
(25) Stachowiak, J. C.; Richmond, D. L.; Li, T. H.; Liu, A. P.; Parekh, S. H.; Fletcher, D. A. Unilamellar Vesicle Formation and Encapsulation by Microfluidic Jetting. *Proceedings of the National Academy of Sciences* **2008**, *105* (12), 4697–4702. https://doi.org/10.1073/pnas.0710875105.
(26) Richmond, D. L.; Schmid, E. M.; Martens, S.; Stachowiak, J. C.; Liska, N.; Fletcher, D. A. Forming Giant Vesicles with Controlled Membrane Composition, Asymmetry, and Contents. *Proceedings of the National Academy of Sciences* **2011**, *108* (23), 9431–9436. https://doi.org/10.1073/pnas.1016410108.
(27) Deshpande, S.; Caspi, Y.; Meijering, A. E. C.; Dekker, C. Octanol-Assisted Liposome Assembly on Chip. *Nat Commun* **2016**, *7* (1), 10447. https://doi.org/10.1038/ncomms10447.
(28) Abkarian, M.; Loiseau, E.; Massiera, G. Continuous Droplet Interface Crossing Encapsulation (cDICE) for High Throughput Monodisperse Vesicle Design. *Soft Matter* **2011**, *7* (10), 4610–4614. https://doi.org/10.1039/c1sm05239j.
(29) Van de Cauter, L.; Fanalista, F.; van Buren, L.; De Franceschi, N.; Godino, E.; Bouw, S.; Danelon, C.; Dekker, C.; Koenderink, G. H.; Ganzinger, K. A. Optimized cDICE for Efficient Reconstitution of Biological Systems in Giant Unilamellar Vesicles. *ACS Synth. Biol.* **2021**, *10* (7), 1690–1702. https://doi.org/10.1021/acssynbio.1c00068.
(30) Blosser, M. C.; Horst, B. G.; Keller, S. L. cDICE Method Produces Giant Lipid Vesicles under Physiological Conditions of Charged Lipids and Ionic Solutions. *Soft Matter* **2016**, *12* (35), 7364–7371. https://doi.org/10.1039/c6sm00868b.
(31) Deek, J.; Maan, R.; Loiseau, E.; Bausch, A. R. Reconstitution of Composite Actin and Keratin Networks in Vesicles. *Soft Matter* **2018**, *14* (10), 1897–1902. https://doi.org/10.1039/C7SM00819H.
(32) Keber, F. C.; Loiseau, E.; Sanchez, T.; DeCamp, S. J.; Giomi, L.; Bowick, M. J.; Marchetti, M. C.; Dogic, Z.; Bausch, A. R. Topology and Dynamics of Active Nematic Vesicles. *Science* **2014**, *345* (6201), 1135–1139. https://doi.org/10.1126/science.1254784.
(33) Litschel, T.; Ganzinger, K. A.; Movinkel, T.; Heymann, M.; Robinson, T.; Mutschler, H.; Schwille, P. Freeze-Thaw Cycles Induce Content Exchange between Cell-Sized Lipid Vesicles. *New J. Phys.* **2018**, *20*, 055008. https://doi.org/10.1088/1367-2630/aabb96.
(34) Litschel, T.; Ramm, B.; Maas, R.; Heymann, M.; Schwille, P. Beating Vesicles: Encapsulated Protein Oscillations Cause Dynamic Membrane Deformations. *Angew. Chem. Int. Ed.* **2018**, *57* (50), 16286–16290. https://doi.org/10.1002/anie.201808750.
(35) Barkley, D.; Henderson, R. D. Three-Dimensional Floquet Stability Analysis of the Wake of a Circular Cylinder. *J. Fluid Mech.* **1996**, *322*, 215–241. https://doi.org/10.1017/S0022112096002777.
(36) Christopher, G. F.; Noharuddin, N. N.; Taylor, J. A.; Anna, S. L. Experimental Observations of the Squeezing-to-Dripping Transition in T-Shaped Microfluidic Junctions. *Phys. Rev. E* **2008**, *78* (3), 036317. https://doi.org/10.1103/PhysRevE.78.036317.
(37) De Menech, M.; Garstecki, P.; Jousse, F.; Stone, H. A. Transition from Squeezing to Dripping in a Microfluidic T-Shaped Junction. *J. Fluid Mech.* **2008**, *595*, 141–161. https://doi.org/10.1017/S002211200700910X.
(38) Stone, H. A. Dynamics of Drop Deformation and Breakup in Viscous Fluids. *Annu. Rev. Fluid Mech.* **1994**, *26*, 65–102. https://doi.org/10.1146/annurev.fl.26.010194.000433.

(39) Janssen, P. J. A.; Anderson, P. D. Boundary-Integral Method for Drop Deformation between Parallel Plates. *Physics of Fluids* **2007**, *19* (4), 043602. https://doi.org/10.1063/1.2715621.
(40) Komrakova, A. E.; Shardt, O.; Eskin, D.; Derksen, J. J. Lattice Boltzmann Simulations of Drop Deformation and Breakup in Shear Flow. *International Journal of Multiphase Flow* **2014**, *59*, 24–43. https://doi.org/10.1016/j.ijmultiphaseflow.2013.10.009.
(41) Ganzinger, K. A.; Merino-Salomón, A.; García-Soriano, D. A.; Butterfield, A. N.; Litschel, T.; Siedler, F.; Schwille, P. FtsZ Reorganization Facilitates Deformation of Giant Vesicles in Microfluidic Traps**. *Angew. Chem. Int. Ed.* **2020**, *59* (48), 21372–21376. https://doi.org/10.1002/anie.202001928.
(42) Loiseau, E.; Schneider, J. A. M.; Keber, F. C.; Pelzl, C.; Massiera, G.; Salbreux, G.; Bausch, A. R. Shape Remodeling and Blebbing of Active Cytoskeletal Vesicles. *Sci. Adv.* **2016**, *2* (4), e1500465. https://doi.org/10.1126/sciadv.1500465.
(43) Berry, J. D.; Neeson, M. J.; Dagastine, R. R.; Chan, D. Y. C.; Tabor, R. F. Measurement of Surface and Interfacial Tension Using Pendant Drop Tensiometry. *Journal of Colloid and Interface Science* **2015**, *454*, 226–237. https://doi.org/10.1016/j.jcis.2015.05.012.
(44) Baldursdottir, S. G.; Fullerton, M. S.; Nielsen, S. H.; Jorgensen, L. Adsorption of Proteins at the Oil/Water Interface—Observation of Protein Adsorption by Interfacial Shear Stress Measurements. *Colloids and Surfaces B: Biointerfaces* **2010**, *79* (1), 41–46. https://doi.org/10.1016/j.colsurfb.2010.03.020.
(45) Mitropoulos, V.; Mütze, A.; Fischer, P. Mechanical Properties of Protein Adsorption Layers at the Air/Water and Oil/Water Interface: A Comparison in Light of the Thermodynamical Stability of Proteins. *Advances in Colloid and Interface Science* **2014**, *206*, 195–206. https://doi.org/10.1016/j.cis.2013.11.004.
(46) Gicquaud, C.; Chauvet, J.-P.; Grenier, G.; Tancrède, P.; Coulombe, G. Adsorption of Actin at the Air-Water Interface: A Monolayer Study. *Biopolymers* **2003**, *70* (3), 289–296. https://doi.org/10.1002/bip.10475.
(47) Gicquaud, C.; Chauvet, J.-P.; Tancrède, P. Surface Film Pressure of Actin: Interactions with Lipids in Mixed Monolayers. *Biochemical and Biophysical Research Communications* **2003**, *308* (4), 995–1000. https://doi.org/10.1016/S0006-291X(03)01505-5.
(48) Schroer, C. F. E.; Baldauf, L.; van Buren, L.; Wassenaar, T. A.; Melo, M. N.; Koenderink, G. H.; Marrink, S. J. Charge-Dependent Interactions of Monomeric and Filamentous Actin with Lipid Bilayers. *Proc Natl Acad Sci USA* **2020**, *117* (11), 5861–5872. https://doi.org/10.1073/pnas.1914884117.
(49) Magnaudet, J.; Mercier, M. J. Particles, Drops, and Bubbles Moving Across Sharp Interfaces and Stratified Layers. *Annu. Rev. Fluid Mech.* **2020**, *52* (1), 61–91. https://doi.org/10.1146/annurev-fluid-010719-060139.
(50) Amador, G. J.; van Dijk, D.; Kieffer, R.; Aubin-Tam, M.-E.; Tam, D. Hydrodynamic Shear Dissipation and Transmission in Lipid Bilayers. *Proc. Natl. Acad. Sci. U.S.A.* **2021**, *118* (21), e2100156118. https://doi.org/10.1073/pnas.2100156118.
(51) Baldauf, L.; Frey, F.; Perez, M. A.; Idema, T.; Koenderink, G. H. *Reconstituted Branched Actin Networks Sense and Generate Micron-Scale Membrane Curvature*; preprint; Biophysics, 2022. https://doi.org/10.1101/2022.08.31.505969.
(52) Schindelin, J.; Arganda-Carreras, I.; Frise, E.; Kaynig, V.; Longair, M.; Pietzsch, T.; Preibisch, S.; Rueden, C.; Saalfeld, S.; Schmid, B.; Tinevez, J.-Y.; White, D. J.; Hartenstein, V.; Eliceiri, K.; Tomancak, P.; Cardona, A. Fiji: An Open-Source Platform for Biological-Image Analysis. *Nat Methods* **2012**, *9* (7), 676–682. https://doi.org/10.1038/nmeth.2019.